PRIFYSGOL BANGOR / BANGOR UNIVERSITY

Observational energy transfers of a spiral cold filament within an anticyclonic eddy

Qiu, Chunhua; Yang, Zihao; Feng, Ming; Rippeth, Tom; Shang, Xiaodong; Sun, Zhenyu; Jing, Chunsheng; Wang, Dongxiao; Yang, Jun

Progress in Oceanography

DOI:
https://doi.org/10.1016/j.pocean.2023.103187

Published: 01/01/2024

Peer reviewed version

Cyswllt i'r cyhoeddiad / Link to publication

Dyfyniad o'r fersiwn a gyhoeddwyd / Citation for published version (APA):
Qiu, C., Yang, Z., Feng, M., Rippeth, T., Shang, X., Sun, Z., Jing, C., Wang, D., & Yang, J. (2024). Observational energy transfers of a spiral cold filament within an anticyclonic eddy. *Progress in Oceanography*, *220*. https://doi.org/10.1016/j.pocean.2023.103187

Hawliau Cyffredinol / General rights
Copyright and moral rights for the publications made accessible in the public portal are retained by the authors and/or other copyright owners and it is a condition of accessing publications that users recognise and abide by the legal requirements associated with these rights.

• Users may download and print one copy of any publication from the public portal for the purpose of private study or research.
• You may not further distribute the material or use it for any profit-making activity or commercial gain
• You may freely distribute the URL identifying the publication in the public portal ?

Take down policy
If you believe that this document breaches copyright please contact us providing details, and we will remove access to the work immediately and investigate your claim.

27. Apr. 2024

Observational energy transfers of a spiral cold filament within an anticyclonic eddy

Chunhua Qiu[1,2], Zihao Yang[1,2], Ming Feng[3], Jun Yang[1,2], Tom P. Rippeth[4], Xiaodong Shang[5], Zhenyu Sun[6], Chunsheng Jing[7] , Dongxiao Wang[1,2,*]

1.School of Marine Sciences, Sun Yat-sen University, and Southern Marine Science and Engineering Guangdong Laboratory (Zhuhai), Zhuhai, 519020, China

2. Guangdong Provincial Key Laboratory of Marine Resources and Coastal Engineering, School of Marine Sciences, Sun Yat-sen University, Guangzhou 510275, China

3. Commonwealth Scientific and Industrial Organization, Australia

4. School of Ocean Sciences, Bangor University, Menai Bridge, Ynys Môn, LL59 5AB, United Kingdom

5. South China Sea Institution of Oceanology, Chinses Academy of Science, Guangzhou, 510301, China

6. State Key Laboratory of Marine Environmental Science, College of Oceanography and Environmental Science, Xiamen University, Xiamen, China

7. Fujian Provincial Key Laboratory of Marine Physical and Geological Processes, Third Institute of Oceanography, Ministry of Natural Resources, China

Corresponding author:

Dr.Prof. Dongxiao Wang

School of Marine Sciences,

Sun Yat-sen University,

Guangzhou 510275, China

Email: dxwang@mail.sysu.edu.cn

Highlights:

- A spiral filament with high chlorophyll-a and low-temperature in an anticyclone was observed using remote sensing and shipboard data;
- The filament was associated with strong vertical velocity, producing a significant secondary circulation, and enhanced turbulent KE dissipation rates;
- The enhanced turbulent KE dissipation rates within filament were mainly controlled via centrifugal and symmetric instabilities.

Abstract

The ocean surface mixed layer represents a critical interface linking the ocean and atmosphere. The physical processes determining the surface mixed layer properties and mediate atmosphere-ocean exchange. Submesoscale processes play a key role in cross-scale oceanic energy transformation and the determination of surface mixed-layer properties, including the enhancement of vertical nutrient transport, leading to increased primary productivity. Herein, we presented observations of the spiral chlorophyll-a filament and its influence on turbulence within an anticyclonic eddy in the western South China Sea during August 2021. The filament had a negative Ertel potential vorticity associated with strong upwelled/downward currents (approximately 20-40 m/day). Across-filament sections of the in-situ profiles showed turbulent dissipation rates enhanced in the filament. We suggested this enhancement values can be attributed to submesoscale processes, which accounted for 25% of the total parameterized turbulent dissipation rates. The present parametrized submesoscale turbulent scheme overestimated the in-situ values. The filament transferred kinetic energy upward to anticyclonic eddy via barotropic instability and gained energy from the anticyclonic eddy via baroclinic instability. After kinetic energy budget diagnostic, we suggested besides symmetric instability, centrifugal instability and mixed layer baroclinic instability should also be included in the turbulence scheme to overcome the overestimation. The observed dual energy transfers between the anticyclonic eddy and filament, and the observed high turbulent energy dissipation within the filament, emphasized the need for these processes to be accurately parameterized regional and climate models.

Keywords: barotropic instability; filament; turbulence; surface mixed layer; South China Sea

---

ADCP: acoustic doppler current profiler; AE: anticyclonic eddy; AVISO: Archiving, Validation, and Interpretation of Satellite Oceanographic; BFLUX: buoyancy flux; CI: centrifugal instability; CTD: conductivity-temperature-depth; ECMRWF: European Center for Medium-Range Weather Forecasts; ERA5: ECMWF Reanalysis v5; GI: gravitational instability; GSP: geostrophic shear production; HSR: horizontal shear production; KE: kinetic energy; MLI: multi-layer baroclinic instability; MVP: moving vessel profiler; PV: potential vorticity; SCS: South China Sea; SI:

symmetric instability; SLA: sea level anomaly; SML: Surface mixed layer; VMP: vertical microstructure profiler; COARE: coupled ocean–atmosphere response experiment

1 Introduction

In this study, we presented novel observations of a surface mixed layer from the South China Sea (SCS), the largest semi-enclosed marginal sea in the Western Pacific Ocean. The upper layer of the SCS experiences cyclonic circulation in winter and anticyclonic currents in summer as a consequence of monsoon (Chu et al., 1999). The western SCS has a western boundary current, zonal offshore jet, and a double gyre or eddy pair in summer (Fang et al., 2002; Hu et al., 2011; Zu et al., 2020). It has been suggested that the jet and dipole are influenced by southwesterly winds (Xu et al., 2008), the balance of topography and wind stress (Gan and Qu, 2008), or barotropic Rossby wave adjustment (Bayler and Liu, 2008). Consequently, the western SCS is a rich zone for multi-scale oceanic motions.

Submesoscale processes (Rossby number, $R_o \approx 1$), such as filaments, submesoscale eddies, and submesoscale fronts, are parts of the energy cascade from mesoscale eddies to smaller-scale motions (e.g., D'Asaro et al., 2011). Filaments result from stirring and straining of mesoscale eddies (Gula et al., 2014), and appear as circular, eddy core, cat's-eye, and spiral patterns (e.g., Ni et al., 2021; Zhang and Qiu, 2020). These filaments have an enhanced vertical velocity (O (10 -100) m/day; Capet et al., 2008; Ruiz et al., 2019), introduce nutrient-rich deeper water into the surface mixed layer (SML), and influence the primary production (Lehahn et al., 2007) and sea surface temperature through vertical heat transport (Su et al., 2020). Consequently, within cold or warm filaments, the submesoscale process modulates the air-sea heat fluxes (Song et al., 2022), influencing climate variability (Wang et al., 2022). Therefore, the characterization of these features is of great interest.

Submesoscale currents can be triggered by symmetric instability (*SI*), mixed-layer baroclinic instability (*MLI*), centrifugal instability (*CI*), and frontogenesis processes (McWilliams, 2016). The *SI* is a two-dimensional roll that occurs in strongly velocitysheared environments (Stone, 1972; Emanuel, 1979). *CI* is one of the barotropic instabilities induced by the curvature of streamlines and can induce strong vertical velocity (Mcwilliams, 2016), whereas *MLI* decreases the isopycnal slope and converts horizontal buoyancy gradients into vertical stratification (i.e., restratification; Boccalett et al., 2006; Gula et al. 2022). Submesoscale processes were found to transfer kinetic energy (KE) to smaller scales via *SI* and transfer energy to mesoscale processes via *MLI* (Fox-Kemper et al., 2008; Dong et al., 2021; Jing et al., 2021). Within a mesoscale eddy, submesoscale processes can develop on the eddy edge (Brannigan et al., 2017), as shown by drifting buoy in SCS (e.g., Qiu et al., 2022), resulting in the transfer of energy at the edge of the mesoscale eddy (e.g., Legg et al., 1988; Thomas et al., 2013； Brannigan et al., 2017). Submesoscale instability at eddy edges have been intensively studied in the SCS (Qiu et al., 2019; Lin et al., 2020; Qiu et al., 2022). These include frontogenesis (Zhong et al., 2017; Dong and Zhong, 2018), *MLI* (Huang et al., 2020; Zhang et al., 2021; Tang et al., 2023), and *SI* (Dong et al., 2022). Enhanced turbulent dissipation rates have been observed at the edges of mesoscale eddies (Yang et al., 2017, 2019; Qi et al., 2020).

Inward spiral structures have been observed using satellite images traced by a high chlorophyll-a concentration belt (Zhang and Qiu, 2020). This type of filament is entrained from the outside towards the eddy centre, and may be generated by a vortex Rossby wave analogous to an atmospheric cyclone (Montgomery and Enagonio,1998; Möller and Montgomery, 1999, 2000), or by a strong vertical velocity or mixing. The different structures are related to the eddy life stage, strength, and background flow field (Melander et al., 1987; Zhang and Qiu,2020; Qiu et al., 2022b). Two-dimensional surface structures of spiral filaments are evident in satellite images and drifter tracks; however, the details of the three-dimensional fine structure and the related energy transfers are still unclear owing to the sparsity of in situ measurements.

Herein, we reported a novel set of observations of the fine structure of a spiral filament within an anticyclonic eddy (AE) and estimated the energy transfer. We found the filament is associated with strong vertical velocities and high turbulent dissipation rates. It gains energy from mesoscale eddies via barotropic instability and transfers energy upward to the mesoscale eddy via *CI*. The application of a turbulent parameterization scheme to the observations shows that the high turbulent dissipation rates coinciding with the filament implies that they are a result of submesoscale processes rather than air-sea buoyancy loss.

2 Data and methods

2.1 Data Sources

Between August 10th and 25th, 2021, an R/V cruise were emplaced by "Xiangyanghong 3" in the western South China Sea (WSCS), within the zone 111.5-113.5°E and 11.5-13.5°N. Turbulence profiles were measured at six stations (black dots in Fig. 1b), using a vertical microstructure profiler (VMP-2000). The instrument provides a velocity shear microstructure from which the profiles of the turbulent dissipation rate are calculated. The VMP acquired shear signals at a sampling frequency of 512 Hz via two probes equipped with shear sensors, and temperature and salinity data were collected at 64 Hz using an SBE conductivity temperature system (Fer et al., 2014). The instrument fell freely to the expected depth at a speed of 0.75 m/s, during which time the shear data were transmitted through the winch cable. The velocity microstructure data were combined with the Nasmyth spectrum to calculate instantaneous estimates of the dissipation for each probe, and the results from the two probes were compared to ensure the reliability of the turbulence observations (Wolk et al., 2002).

An AML oceanographic moving vessel profiler 300 (MVP300) consists of an electric winch system, a PC control unit, a towed vehicle that is equipped with conductivity-temperature-depth (CTD) sensors (https://geo-matching.com/uploads/default/m/v/mvp-data-sheet-211005-0.pdf). It has been used to collect high-resolution temperature, salinity, and depth profile by CTD, while the voyage was underway at a mean speed of 6 knot from August 18th to August 22nd. The

MVP300 fell freely at approximately 2 m/s from surface to 200 m depth and returned to the surface via winch. The CTD sensors on the MVP300 may be affected by conductivity time lag, thermal mass, the speed of probe, and so on (L'Hégaret et al., 2023). We used the downward temperature and salinity profiles with a horizontal resolution of 1~ 2 km, which is sufficiently fine enough to identify submesoscale processes. Before the cruise, we have calibrated the temperature and conductivity sensors on MVP300 in national center of ocean standards and metrology (NCOSM), China, which acts as the WMO-IOC Regional Marine Instrument Center for the Asia-Pacific from 2012 and mainly takes charge of national ocean standardization, metrology and quality supervision. After calibration, the accuracies of temperature and conductivity are 0.003°C and 0.003 mS/cm, respectively. As a successful underway measurement, the MVP300 has captured submesoscale processes in many previous studies (e.g., Taylor et al., 2018; Shao et al., 2019; Song et al., 2022).

A vessel-mounted acoustic doppler current profiler (ADCP) was used to measure the current velocity profiles. The 300 kHz ADCP provides current velocities with a 2-m vertical resolution over a depth range of 580 m. Weather information was collected using a XZC6-1 marine automatic weather instrument installed at the height of 18 m from the sea surface, which provided air temperature, humidity, wind velocity, and air pressure with temporal resolution of 1-min. The wind speed at a height of 10 m was derived using the coupled ocean–atmosphere response experiment (COARE 3.0) algorithm, which was determined by the logarithmic profiles (https://www.pmel.noaa.gov/ocs/flux-documentation).

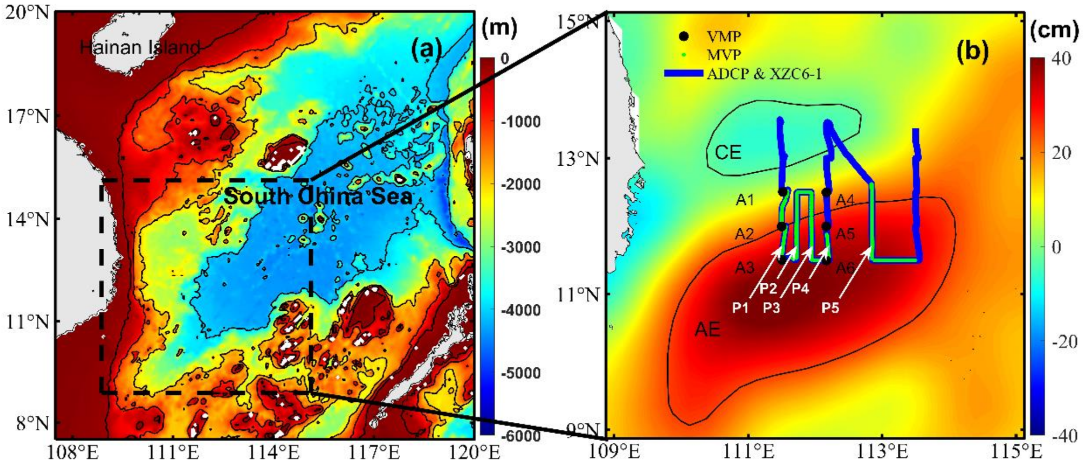

Figure 1. (a) Topography of the South China Sea. (b) Observation sites superimposed sea level anomaly (unit: cm). The black dots are the observation stations of VMP, the blue lines are the ship track, and the green lines superimposed the blue lines are the underway MVP tracks. Transections of P1, P2, P3, P4 and P5 are from west to the east.

Daily sea level anomaly (SLA) data with a spatial resolution of 0.25° from the Archiving, Validation, and Interpretation of Satellite Oceanographic (AVISO) project were used to identify mesoscale eddies. AVISO integrates several satellite products including JASON-1, TOPEX/Poseidon, ERS-1/ERS-2.

The European Centre for Medium-Range Weather Forecasts (ECMWF) Reanalysis v5 (ERA5) provides information on the evaporation, precipitation, short-wave radiation, long-wave radiation, effective wave height, and mean wave period, which were used to parameterize the turbulent dissipation rates. We selected the voyage time spanning from August 10th to 25th, 2021. The spatial resolution of the data was 0.25^{o}, except for waves, which had a resolution of 0.5^{o}; and the temporal resolution was 1 hour. We gridded the above data to a horizontal resolution of 2 km and vertical resolution of 2 m.

We used the level-2 chlorophyll-a products from visible and infrared imager/radiometer suite (VIIRS) onboard the Suomi-NPP satellite. The spatial resolution of these data is approximately 0.75 km × 0.75 km, and the temporal resolution has a range of several hours. We mapped the valid data points onto a 1 km × 1 km grid using the inverse distance weighting interpolation method.

2.2 Surface Turbulence Parameterization Scheme

Turbulence in the ocean SML can be generated by three processes: waves and wind, buoyancy loss, and submesoscale motions. Following Buckingham et al. (2019), we assumed the total turbulent dissipation rate, ε_{Σ}, is a superposition of three contributions,

$$\varepsilon_{\Sigma} = \varepsilon_{sw} + \varepsilon_{b} + \varepsilon_{sm} \ , \tag{1}$$

where ε_{sw}, ε_{b}, and ε_{sm} are the generated turbulence induced by waves and wind, buoyancy loss and submesoscale, respectively.

2.2.1 Parameterized turbulence due to surface buoyancy fluxes

The turbulent dissipation rate owing to buoyant forced convection is parameterized as a function of depth z,

$$\varepsilon_b = \begin{cases} B_o(\frac{z+h}{h}), & B_o > 0 \ and \ 0 < |z| \le h, \\ 0, & B_o \le 0 \ or \ |z| > h. \end{cases} \tag{2}$$

Here, h is the depth of forced convection at the ocean surface. When the water depth was greater than h, the turbulence generated by the surface buoyancy flux was ignored. The buoyancy fluxes, B_o, was related to air-sea heat and freshwater fluxes (Jensen,2016). The latent and sensible heat fluxes were calculated with the COARE 3.0 algorithm using the in-situ air temperature, humidity, and wind speed.

Convective layer depth h is expressed as follows (Taylor and Ferrari, 2010):

$$\begin{cases} z'^4 - c^3(1-z')^3 \left[\frac{B_o H}{\left|\frac{\nabla_h b}{f}\right|^3 H^3} + \frac{\frac{|\tau|\cos\theta}{\rho_o}}{\left|\frac{\nabla_h b}{f}\right|^2 H^2} \right]^2 = 0, \\ z' = \frac{h}{H}. \end{cases} \tag{3}$$

H is the depth of the mixed layer at which the temperature exceeds 0.5 $^{o}\mathrm{C}$ compared to the density at 10-m depth. The buoyancy, $b = g(1 - \rho/\rho_o)$, is calculated based on the density ρ and the reference density ($\rho_o = 1025\ \mathrm{kg}/m^3$), and $\nabla_h b$ is the average buoyancy gradient within 20 m. c =13.9 is the empirical coefficient, and f is the Coriolis parameter. The geostrophic component of the wind, $|\tau|\cos\theta$, is determined by wind stress $\boldsymbol{\tau}$ and angle θ of the wind relative to the geostrophic velocity direction.

2.2.2 Parameterized turbulence due to waves and wind

The effects of waves and wind on turbulence occurs through wave breaking and current shear (Buckingham et al., 2019). Taking the Langmuir turbulence into account, the turbulence parameterization of the ocean surface can be derived (Belcher et al., 2012). The ocean was then divided into three layers using transition depth z_L and H. In the outermost layers of the ocean ($0 < |z| \le |z_L|$), waves dominate; in the second layer ($|z_L| < |z| \le H$), Langmuir turbulence is the primary contributing factor on the turbulent dissipation rate. When the depth is greater than H, the effects of waves and wind are ignored, and the corresponding turbulent dissipation rate is considered to be zero.

$$\varepsilon_{sw} = \begin{cases} 0.03u_w^2 \frac{H_s}{z^2}\frac{gT}{2\pi}, & 0 < |z| \le |z_L| \\ 0.23\frac{u_w^2 u_s}{|z|}(1 - 0.6\frac{z}{h}), & |z_L| < |z| \le H \\ 0, & |z| > H, \end{cases} \tag{4}$$

where u_w is the waterside friction velocity, H_s is the significant wave height, T is the average period of the wave, and $u_s = \frac{u_w}{La^2}$ is the surface Stokes drift velocity. To simplify the calculation of Stokes drift velocity, the turbulent Langmuir number $La = \sqrt{\frac{u_w}{u_s}} = 0.3$ is utilized (McWilliams et al., 1997). z_L is calculated as follows,

$$z_L = \frac{5}{6}H\left[1 - \sqrt{1 + \frac{36}{115}\frac{H_s}{H}\frac{1}{u_s}\frac{gT}{2\pi}}\right]. \tag{5}$$

2.2.3 Parameterized turbulence due to submesoscale instability

As mentioned in Buckingham et al. (2019), the turbulence induced by submesoscale instability is mainly related to Ekman induced fluxes and buoyancy fluxes , and is parameterized as:

$$\varepsilon_{sm} = \begin{cases} (B_e + B_o)\left(\frac{z+H}{H}\right) - B_o\left(\frac{z+h}{h}\right), & 0 < |z| \le h \text{ and } B_o + B_e > 0 \\ (B_e + B_o)\left(\frac{z+H}{H}\right), & h < |z| \le H \text{ and } B_o + B_e > 0 \\ 0, & |z| > H \text{ or } B_o + B_e < 0. \end{cases} \tag{6}$$

The calculation of buoyancy flux driven by Ekman transport B_e is as follows,

$$B_e = \left(\frac{\boldsymbol{\tau}\times\boldsymbol{f}}{\rho_o f^2}\right)\cdot\nabla_h b. \tag{7}$$

2.3 Calculation of vertical velocity

Submesoscale processes easily produce a secondary circulation, causing strong vertical velocities, and affecting the local circulation structure (Ruiz et al., 2019; Xuan et al., 2021). As the vertical velocity is quite small in the ocean, it's difficult to be measured directly. The distribution of vertical velocities can be calculated using density conservation equation (Yu et al., 2019; Qiu et al., 2020) and quasi-geostrophic Omega equation (Martin and Richards, 2001). The former method is as follows,

$$\frac{\partial \rho}{\partial \mathrm{t}} + u\frac{\partial \rho}{\partial x} + v\frac{\partial \rho}{\partial y} + w\frac{\partial \rho}{\partial z} = 0, \tag{8}$$

$$w = -\frac{\left(\frac{\partial \rho}{\partial t} + u\frac{\partial \rho}{\partial x} + v\frac{\partial \rho}{\partial x}\right)}{\frac{\partial \rho}{\partial z}}, \tag{9}$$

where u and v were provided by ADCP, ρ was measured by MVP300. Here, we assumed the water density to be constant, i.e., $\frac{\partial \rho}{\partial \mathrm{t}} = 0$. $\frac{\partial \rho}{\partial x} \approx \frac{\Delta \rho}{\Delta x}$ and $\frac{\partial \rho}{\partial \mathrm{y}} \approx \frac{\Delta \rho}{\Delta \mathrm{y}}$ were derived by using central finite difference method.

The vertical velocity from quasi-geostrophic omega equation (Martin and Richards, 2001; Hu et al., 2011) is as follows:

$$f^2\frac{\partial^2 w}{\partial z^2} + N^2\left(\frac{\partial^2}{\partial x^2} + \frac{\partial^2}{\partial y^2}\right)w = \nabla_h Q, \tag{10a}$$

$$Q = \left[2f\left(\frac{\partial v_g}{\partial x}\frac{\partial u_g}{\partial z} + \frac{\partial v_g}{\partial y}\frac{\partial v_g}{\partial z}\right), -2f\left(\frac{\partial u_g}{\partial x}\frac{\partial u_g}{\partial z} + \frac{\partial u_g}{\partial y}\frac{\partial v_g}{\partial z}\right)\right], \tag{10b}$$

where f is the Coriolis parameter, N^2 is the buoyancy frequency, and u_g and v_g are geostrophic velocities.

3 Results

3.1 The appearance of filament within anticyclonic eddy

We used a winding-angle algorithm (Chaigneau et al., 2008) to identify the position and range of the mesoscale eddy. The local maximum SLA value within a range of $1^\circ \times 1^\circ$ was taken as the eddy center. The outermost closed streamline was the eddy edge.

This method was widely used to identify mesoscale eddy in SCS (Chen et al., 2011; Qiu et al., 2022). The AE was centered at (111.5°E, 10.9°N) with a radius of approximately 200 km. A high chlorophyll-a concentration belt, which was taken as "filament" in the AE (Fig. 2) appeared on August 16th, 20th, 21st, and 22nd. The high chlorophyll-a values are usually associated with typically upwelling bands in which nutrients are transported to the surface (Brannigan, 2016; Zheng and Jing, 2022). Subsurface maximum chlorophyll-a were significant in summer in SCS, and the upwelling could bring high chlorophyll-a water to surface (Chen et al., 2022). The eddy filament had the maximum chlorophyll-a concentration on August 20th. Areas of high chlorophyll concentration (tens of kilometers) may be thicker than upwelling band filaments (several kilometers) because of the temporal accumulation of net productivity (Brannigan, 2016).

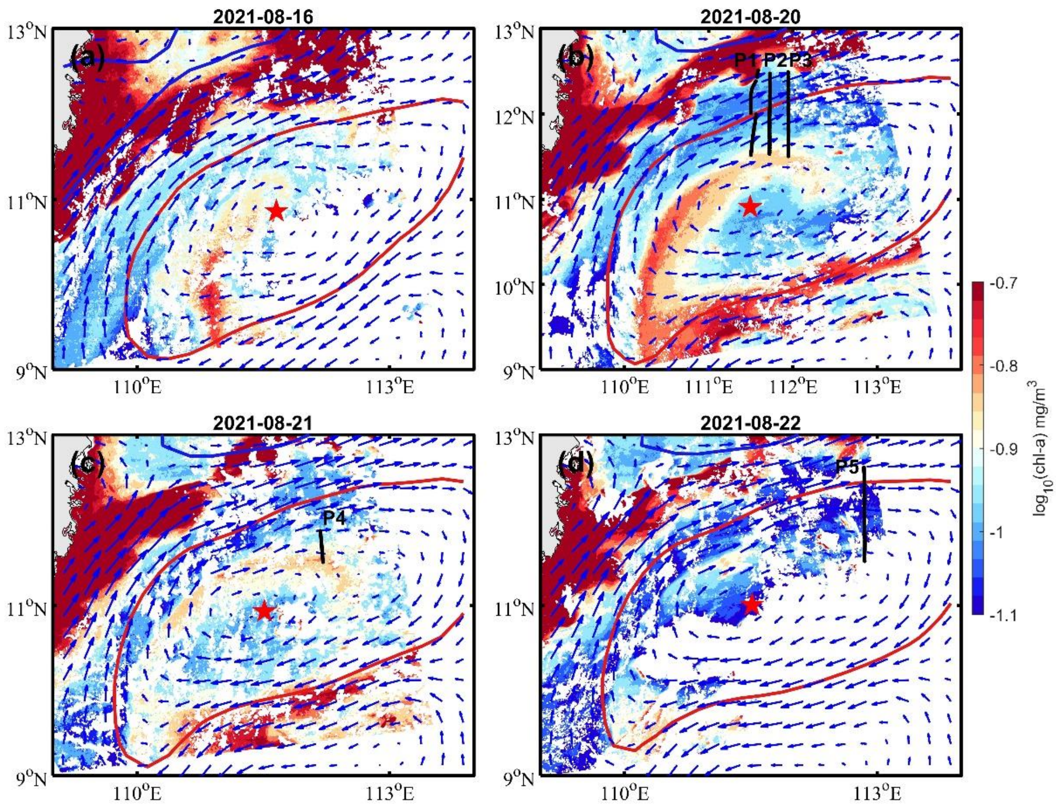

Figure 2. Distribution of chlorophyll-a concentrations (mg/m^3) on August 16th, 20th, 21st, and 22nd, 2021. The red (blue) pentagram and the red (blue) isoclines represent the center and edge of the anticyclonic eddy (cyclonic eddy), respectively. The black lines in (b), (c), and (d) are the tracks of MVP. P1, P2, and P3 observations were conducted on August 19th and 20th. P4 and P5

observations were conducted on August 21st and 22nd. The blue vectors are the geostrophic velocity.

The zonal mean relative vorticity within the anticyclone is shown in Figure 3 to depict the evolution of the AE. The absolute value of relative velocity achieved a stable value of $9 \times 10^{-6}\ \mathrm{s}^{-1}$ from August 15th to 22nd, when the filament appeared on satellite images. From August 23rd to 30th, the filament may also exist, but there were no chlorophyll-a data in this region due to cloud contamination. The results indicated that the strong rotation velocity during AE matured stage may induce the formation of eddy filament. By tracking the mean axis of high chlorophyll-a values, we found the eddy filament shifted approximately 17 km distance at a speed of $\frac{\pi}{8}$ rad/day or 0.5 m/s at the eddy edge from August 16th to August 22nd. Zhang and Qiu (2018; 2020) suggested that the spiral structure of chlorophyll-a may be related to vortex Rossby waves. Although the presence and propagation of vortex Rossby wave cannot be supported by the present observation, it deserves future study in the dynamic relationship between evolution of spiral structure and vortex Rossby wave.

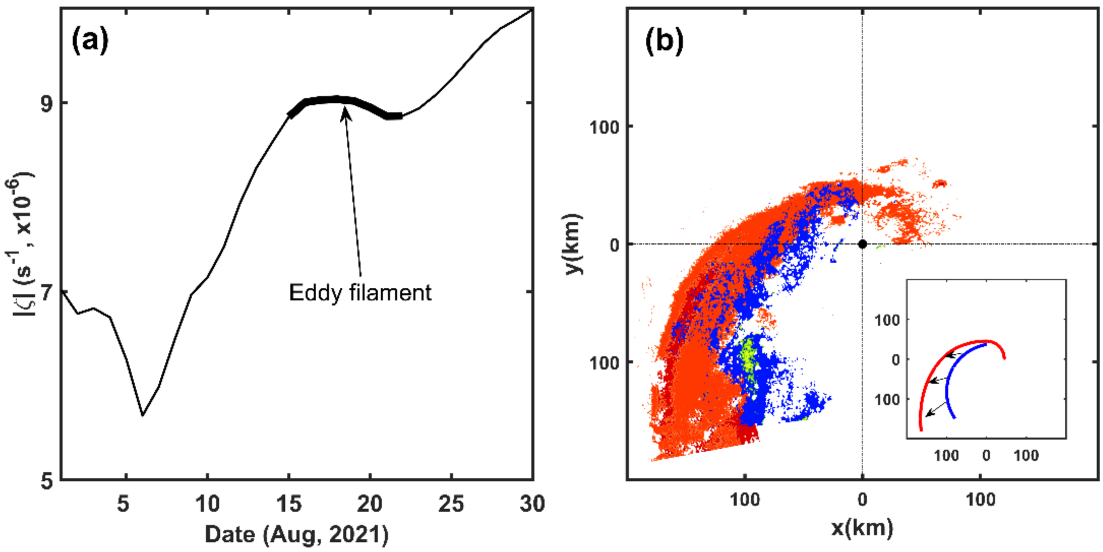

Figure 3. (a) Absolute value of relative vorticity ($|\zeta|$) of the anticyclonic eddy from August 1st, 2021 to 22nd, 2021. The thick line segment represents the time when the eddy filament existed on

satellite images. (b) The shift of the eddy filament zone. The dots and lines in (b) are the positions and mean positions of chlorophyll-a bands (> 1.4 mg/m^3) on August 16th (blue) and 20th (red).

3.2 Three-dimensional structure of the filament

The cross-sectional temperature, salinity, and velocity were measured using MVP and ADCP from August 18th to 22nd, corresponding to the mature stage of the AE. Profiles of P1, P2, and P3 were extracted for analysis, as shown in Figure 4. The results showed that high-salt, low-temperature, and high-density waters were uplifted significantly at a narrow zone (dashed lines in Figure 4), which was named as cold filament in the following and just in the north of chlorophyll-a filament. The cold and high-density filament (potential density > 21 kg/m^3) had a width of 4 km.

Figure 4d showed the distributions of vertical velocity. Both the two methods supported that a significant secondary current appeared with an upwelling velocity in south of the cold filament, and a downwelling velocity to north of the cold filament. The maximum vertical velocity achieved 80 m/day (5 m/day) in the continuity equation (omega equation) method. It confirmed the filament was associated with strong vertical velocity. Note that the vertical velocity from continuity equation is much larger than that from Omega equation. Omega equation is based on balanced motion, and the vertical velocity is an adjustment of quasi-geostrophic motion, while the continuity equation includes many ageostrophic unbalanced motions and may induce large vertical velocity. This was consistent with results from Lin et al (2020), who showed a big difference between the raw vertical velocity and smoothed vertical velocity.

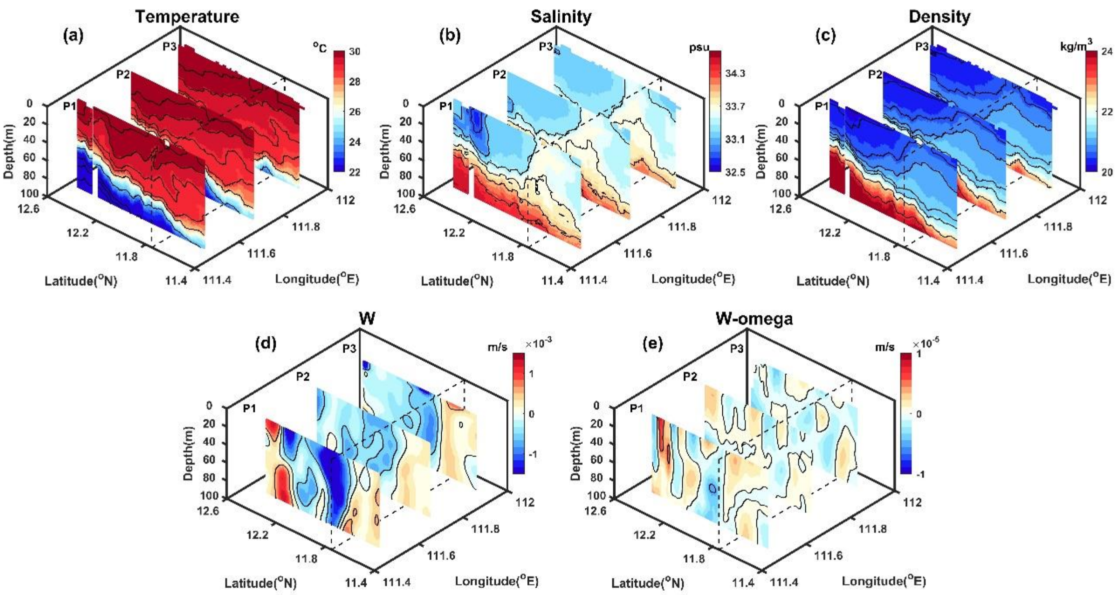

Figure 4. Distributions of (a) temperature (℃), (b) salinity (psu), (c) density (kg/m^3), and vertical velocity (m/s) derived from (d) continuity equation and (e) omega equation at sections P1, P2, and P3. The dashed lines are the position of the cold filament.

The average horizontal velocities within the upper 20 m in the five MVP sections are shown in Figure 5. In the cold filament zone, high velocity shear occurred. Neglecting zonal variations, convergence and divergence can be displayed using the meridional velocity gradient ($\partial v/\partial y$; Fig. 5c). The convergence (divergence) in Fig. 5a could explain the downwelling (upwelling) in the north (south) of the filament (Fig. 4d), and the density fronts with negative(positive) density gradient (Fig.5c) in the north(south) of this filament.

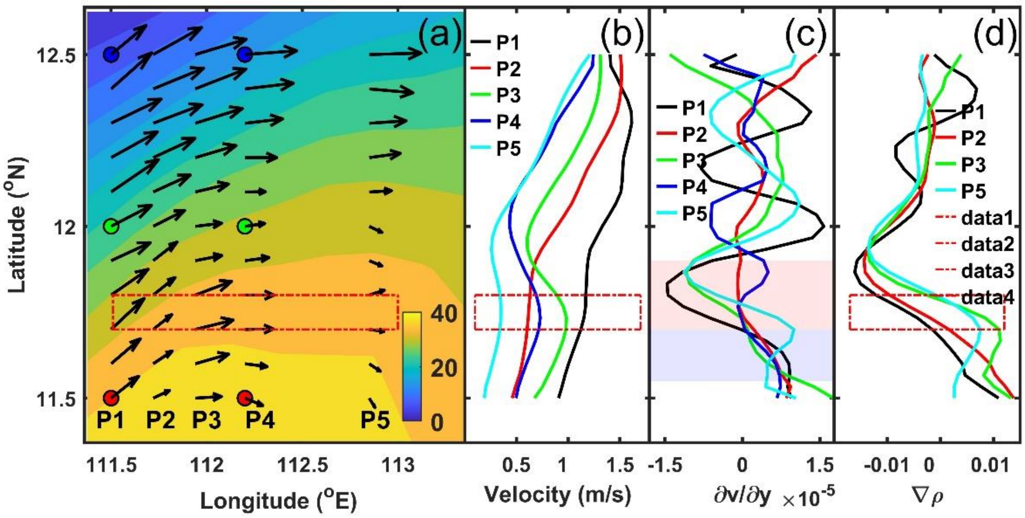

Figure 5. Vertical mean (a) velocity, (b)zonal mean velocity, (c) meridional divergence ($\partial v/\partial y$) and (d) density gradient at 0~20 m. The dashed boxes are the locations of submesoscale filaments. The pink area in (c) represents convergence with negative divergence value, while the blue area represents divergence with positive divergence value. The background color in (a) is the sea level anomaly. Black, red, green, blue, and canyon lines are values at sections of P1, P2, P3, P4, and P5, respectively.

Submesoscale instability plays an important role in energy balance. The buoyancy frequency ($N^2 = -\frac{1}{\rho}\frac{\partial \rho}{\partial z} = b_z$) and Ertel *PV* are shown in Figure 6. When $N^2 < 0$, high-density seawater rises above low-density seawater triggering gravitational instability (*GI*); in our observation, the observation sites of $N^2 > 0$ were popular in the three sections, indicating that most regions were not influenced by *GI*. The Ertel *PV* is defined as, $q = (f\vec{k} + \vec{\varepsilon}) \cdot \nabla b$ (Hoskins, 1974). Instability occurs when q and f have opposing signs, that is, $fq < 0$. For barotropic flows, *CI* satisfies when $f\zeta_{abs}N^2 < 0$ and $N^2 > 0$, where $\zeta_{abs} = f + \zeta$ is the absolute vorticity (Thomas et al., 2013). Ertel *PV* can be divided into a horizontal component, $q_b = (\frac{\partial u}{\partial z})\frac{\partial b}{\partial y}$, and a vertical component, $q_v = (f - \frac{\partial u}{\partial y})\frac{\partial b}{\partial z}$. *SI* obeys the conditions $q < 0$ and $q_v > 0$. Note that $\mathrm{f}\zeta_{abs}N^2 < 0$ appeared in the filament (the dashed box in Fig. 6d-6f), which was attributed to *CI*.

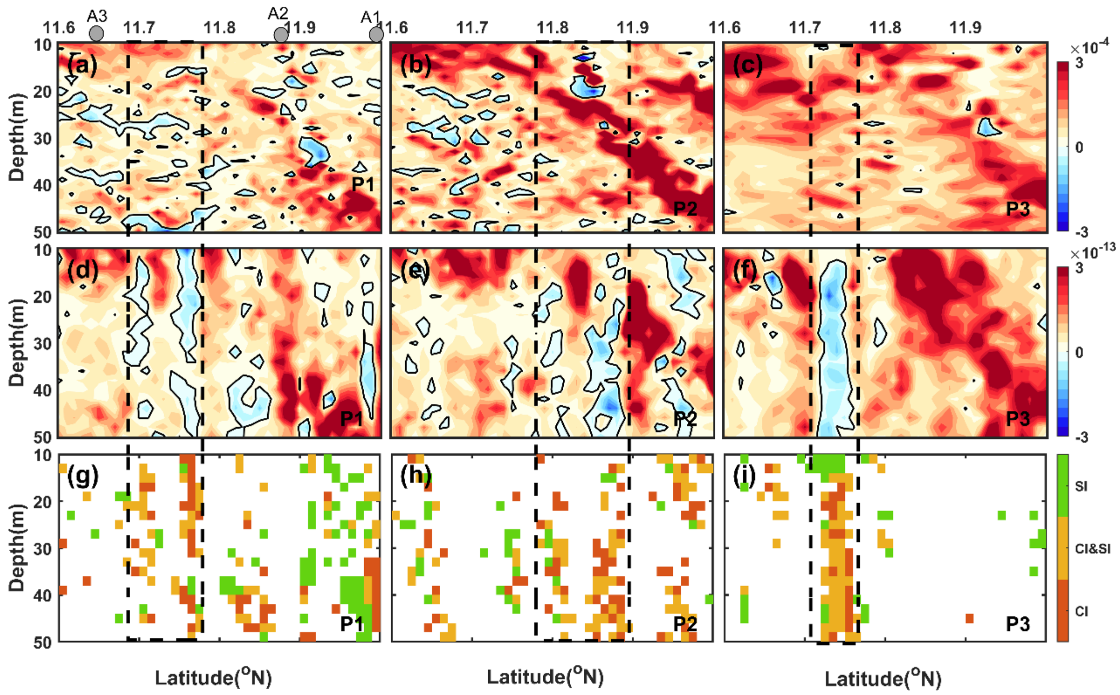

Figure 6. Vertical distribution of buoyancy frequency (N^2, a~c), Ertel *PV* (d~f) and instability division (g~i) for the three sections of P1, P2, and P3. The dashed boxes indicate the positions of the cold filament. Green, yellow and brown in (g-i) represent the centrifugal instability (*CI*), centrifugal or symmetric instability (*CI&SI*), and symmetric instability (*SI*). The grey dots in (a) are positions of A1, A2 and A3 sites.

Following Dong et al. (2022), submesoscale instabilities could be classified as *GI*, *SI*, and *CI* under the following conditions: (a) *CI*: $\zeta < -f$, $b_z > 0$, and $q_b > 0$; (b) *CI&SI*: $\zeta < -f$, $b_z > 0$, and $q_b < 0$; (c) *SI*: $\zeta > -f$, $b_z > 0$, and $q_b < 0$; (d) *SI&GI*: $\zeta > -f$, $b_z < 0$, and $q_b < 0$; and (e) *GI*: $\zeta > -f$, $b_z < 0$, and $q_{bc} > 0$. Figures 6g~6i show that mixed instability of *CI&SI* was the most prominent (50%) in this filament, followed by *CI* (30%).

3.3 Enhanced turbulence associated with the submesoscale filament

Figure 7 shows the vertical distribution of the measured turbulent dissipation rate (background color), estimated wind-wave forced turbulent dissipation rate ε_{sw}, and the submesoscale forced turbulence, ε_{sm}. In the upper 10 m, the in-situ ε in the filament stations (A3) was one order of magnitude larger than that in other regions of the anticyclone. At the depth of 10-20 m, the estimated submesoscale forced turbulent dissipation rate, ε_{sm}, was one order of magnitude larger than the estimated wind and wave-forced turbulent dissipation rates.

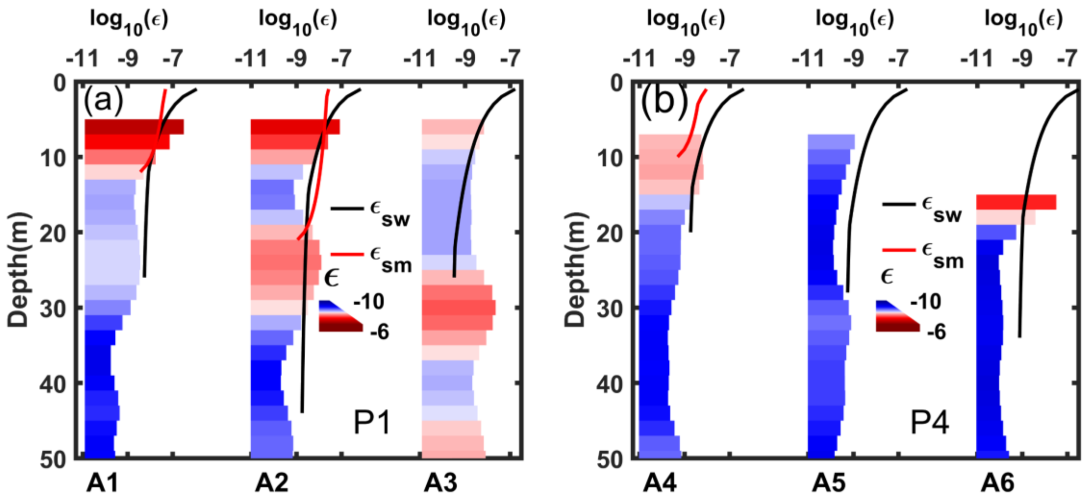

Figure 7. Vertical profiles of turbulent dissipation rates at sections of (a) P1 and (b) P4. The background color is the in-situ turbulent dissipation rate (ε, W/kg). Black lines are the wind-wave forced turbulent dissipation rates (ε_{sw}, W/kg), and red lines are the submesoscale forced turbulent dissipation rate (ε_{sm} , W/kg).

The vertical mean turbulent dissipation rate over depth range 10-20 m along the MVP300 sections is shown in Figures 8a-c. The total turbulent dissipation rate, ε_{Σ}, had a similar pattern as ε_{sw}. In the filament zone (dashed box), ε_{sm} increased to a maximum value of $10^{-7.8}$ W/kg, and accounted for 20~30% of the total estimated turbulent dissipation rate. In contrast, the proportion dropped to zero in the non-filamentous region (12°N-12.5°N). The estimated turbulent dissipation rate, ε_{Σ}, was larger than the in-situ values, indicating that the turbulent parameterization scheme for submesoscale process had overestimated the turbulent dissipation rate.

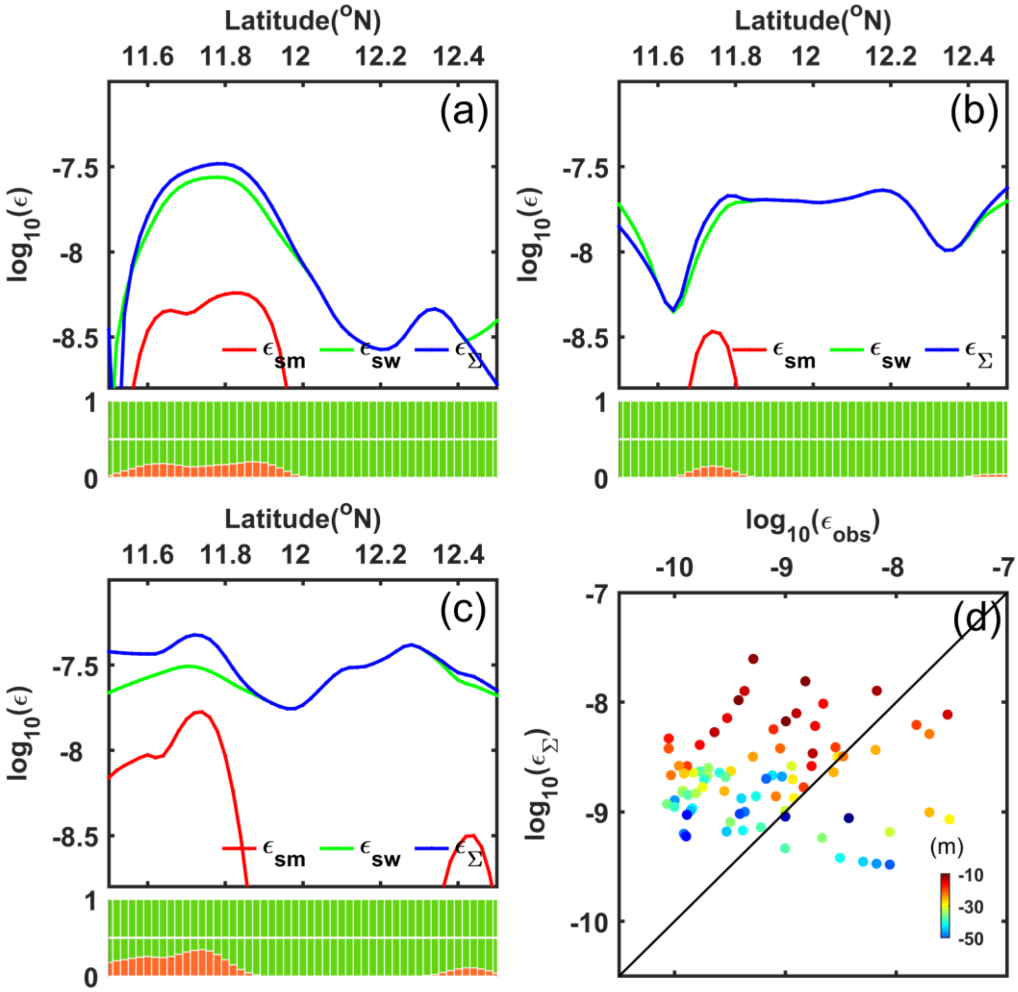

Figure 8. Estimated turbulent dissipation rate from parameterization scheme caused by submesoscale instability, ε_{sm}, wind-wave forced turbulence, ε_{sw}, and total turbulence ε_{Σ}. The Vertical mean turbulent dissipation rates at a depth of 10~20 meters at sections P1, P2, and P3 are shown in (a), (b), and (c), respectively. The histogram is the contribution of ε_{sm} and ε_{sw} to the total turbulence ε_{Σ}. (d) Scatter plots between synthetic turbulent dissipation rates (ε_{Σ}) and in situ turbulent dissipation rates (ε_{obs}). Color dots represent observed depths.

4 Discussion

Submesoscale currents can be generated by *SI*, *MLI*, geostrophic straining-frontogenesis, and turbulent thermal winds (McWilliams, 2016). *SI* usually transfers submesoscale energy to smaller or dissipate scale currents, whereas *MLI* easily transfers energy to larger-scale currents (Srinivasan et al., 2023). The *SI*-forced turbulent dissipation rate overestimated the in-situ value, which may affect the accuracy of air-sea heat flux products. This overestimation may be induced by other submesoscale instabilities, such as *CI* and *MLI*.

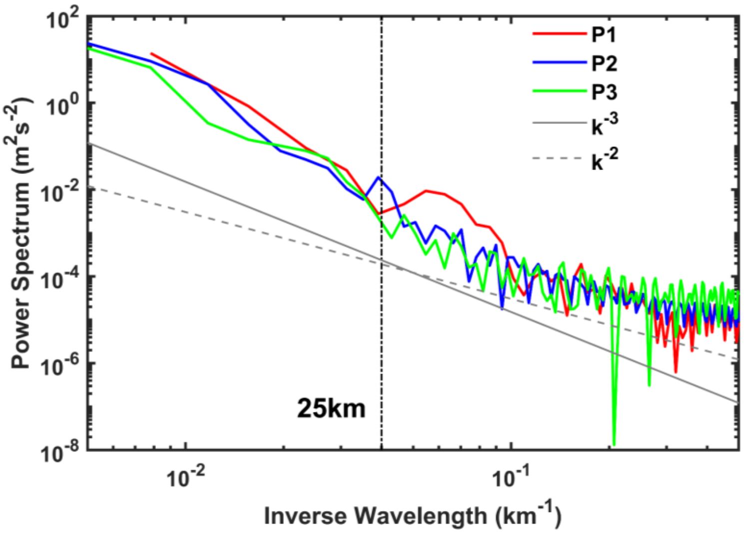

Figure 9. Spectrum analysis of P1 (red line), P2 (blue line) and P3 (green line) sections based on ADCP-measured velocity. The solid gray line is the standard line with slope k^{-3}, and the dashed gray line is the standard line with slope k^{-2}. The dashed black line serves as the dividing line of 25 km between mesoscale and submesoscale motions.

The energy exchange between the AE and filament can be quantified using the four-box energy budget. Following Böning and Budich (1992), baroclinic energy conversion, BC, and barotropic energy conversion, BT, are calculated as follows:

$$BC = -\frac{g}{\rho\left(-\frac{\partial \bar{\rho}_\theta}{\partial z}\right)}\left(\overline{u'\tilde{\rho}'}\frac{\partial \bar{\tilde{\rho}}}{\partial x} + \overline{v'\tilde{\rho}'}\frac{\partial \bar{\tilde{\rho}}}{\partial y}\right), \tag{11}$$

$$BT = -\left(\overline{u'u'}\frac{\partial \bar{u}}{\partial \mathrm{x}} + \overline{u'v'}\left(\frac{\partial \bar{v}}{\partial \mathrm{x}} + \frac{\partial \bar{u}}{\partial \mathrm{y}}\right) + \overline{v'v'}\frac{\partial \bar{v}}{\partial \mathrm{y}}\right). \tag{12}$$

where $(\bar{u}, \bar{v})$ is the mesoscale velocity, and (u', v') is the submesoscale velocity. To isolate the mesoscale and submesoscale processes, we analyzed the KE spectrum following Callies and Ferrari (2013), who suggested that the slopes of k^{-2} and k^{-3} represented submesoscale and mesoscale motions, respectively. As shown in Figure 9, the KE spectrum parallel to the $k^{-2}(k^{-3})$ line interacted at a wavelength of 25 km. Therefore, we defined horizontal scales smaller and larger than 25 km as submesoscale and mesoscale signals, respectively.

Figure 10 shows the baroclinic (BC) and barotropic (BT) energy conversions between mesoscale eddies and submesoscale processes. In the cold filament (dashed box zone), the baroclinic energy conversion was positive (Figs. 10a, 10d and 10g), indicating mesoscale eddy transferred potential energy forward to the filament. The barotropic energy conversion was negative, transferring KE upward to a mesoscale eddy. The net energy conversion term was negative in the filament (Figs. 10c, 10f and 10i), indicating an inverse energy cascade via barotropic instability.

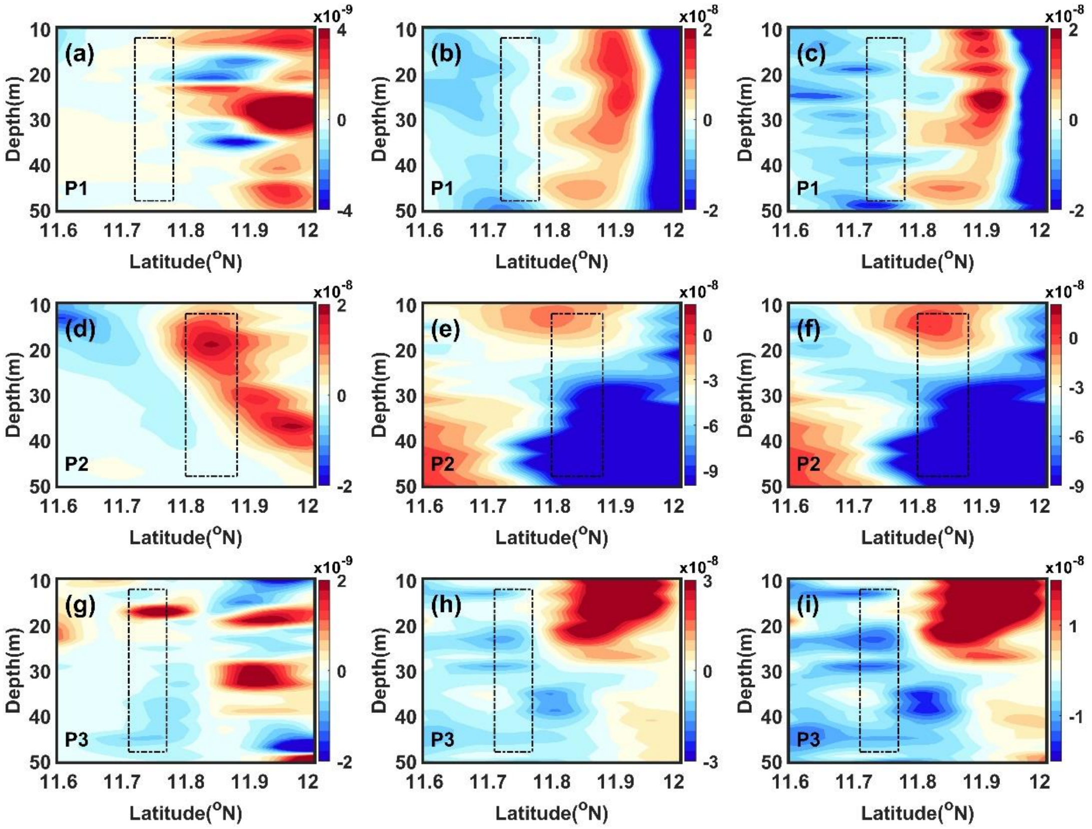

Figure 10. (a), (d) and (g) show the zonal distributions of the baroclinic instability energy conversion; (b), (e), and (h) are the zonal distributions of the barotropic instability energy conversion; (c), (f) and (i) are the net energy conversion. Top to bottom panels are values along P1, P2, and P3 transections, respectively. The black dotted frame indicates the position of the submesoscale cold filament.

We further examined the turbulent KE dissipation rates induced by cross-scale energy conversion, KE_{cs}, following Harrison and Robinson (1978) and Gula et al (2016),

$$\frac{\partial}{\partial t}\mathrm{KE}_{cs} = -\underbrace{\overline{u'_j u'_i}\frac{\partial \overline{u_i}}{\partial x_j}}_{MKE\to EKE} + \underbrace{\overline{w'b'}}_{EPE\to EKE}, \tag{13}$$

Here, primes are the disturbances, and overbars are the mean value. u_j and u_i are the velocities with $j = 1, 2, 3$ and $i = 1, 2$. $BFLUX = \overline{w'b'}$ is the turbulent KE dissipation rate due to the vertical buoyancy flux, representing energy rates induced by *MLI*. w' and b' are the extracted vertical velocity and buoyancy, respectively. $GSP = -\overline{u'w'} \cdot \frac{\partial \bar{u}_g}{\partial z}$ is given by geostrophic shear production, which presents the turbulent KE rates induced by *SI* (Bennetts and Hoskins, 1979), and is taken as the submesoscale generated turbulence in Buckingham et al (2019). We also calculated the energy conversion rate due to horizontal shear production term $HRS = -\overline{\boldsymbol{u}'v'}\frac{\partial \bar{\boldsymbol{u}}}{\partial y}$, representing the turbulent KE rate from *CI*.

As shown in Figure 11, the net energy conversion rates from these three terms ($BFLUX + GSP + HRS$) were positive, indicating the filament dissipated KE to smaller scales. During this process, *HSR* showed negative values at the filament in all the three transections (Figs. 11c, 11g and 11k), which suppressed the KE dissipation rates induced by *GSP*. In the former turbulence scheme (Buckingham et al., 2019), the turbulent dissipation rate induced by *HSR* was not taken into account and thus may cause the overestimation of in situ turbulent value.

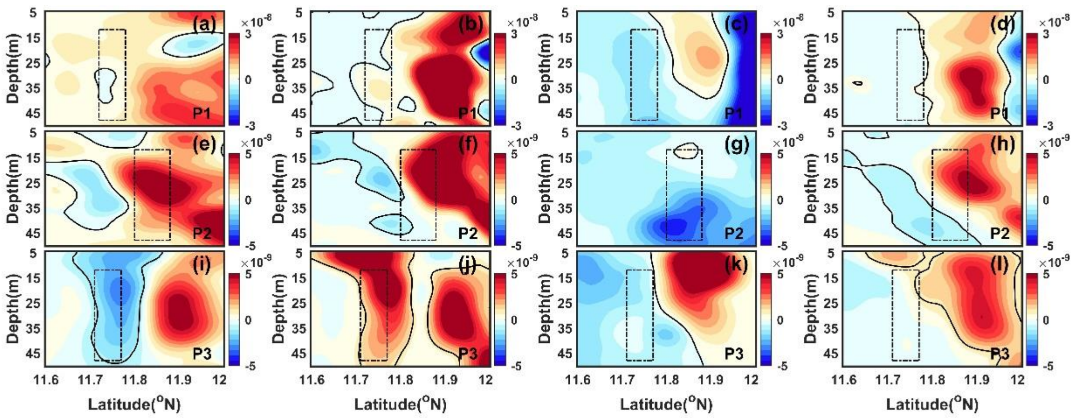

Figure 11. (a), (e), and (i) are the zonal distributions of buoyancy flux (*BFLUX*); (b), (f) and (j) are the zonal distributions of the *GSP*; (c), (g) and (k) are the *HSR* values; (d), (h) and (l) are the sum values of the former three terms. Top to bottom panels are values along P1, P2, and P3

transections, respectively. The black dotted frame circles the position of the submesoscale filaments, and the real line is the zero line.

A structural diagram of energy transfer of the eddy filament in the AE is shown in Figure 12. During the AE matured stage (Fig. 3), *CI* developed (Fig. 6). Both the *HSR* and barotropic energy conversion between the mesoscale and filament were negative, indicating that the *CI* process transferred KE to the AE because of strong horizontal velocity shear. The net energy fluxes of geostrophic vertical shear production and buoyancy fluxes were positive, representing that the filament withdrew KE from the anticyclone through baroclinic instability.

It was suggested that submesoscale process transferred KE to smaller scales via *SI* and transferred energy to mesoscale processes via *MLI* by former studies (Fox-Kemper et al., 2008; Dong et al., 2021; Jing et al., 2021). The length scale that separates the bi-directional KE transfers is controlled by the relative strengths of co-existing balanced and unbalanced motions (Qiu et al., 2022). In this study, we found *MLI* was positive in the filament zone at P2 section, indicating a different direction of KE cascade with former studies. Both the continuity equation and omega equation showed the same distribution of upward and downward motions across the filament, indicating the direction of *MLI*-forced KE cascade was reliable. We presented observational evidence for bi-directional KE transfers of *MLI* and *SI* at submesoscale. The magnitude of *MLI* may have some uncertainties: on the one hand, the calculation of vertical velocity and the spatial and temporal resolution of in situ data may bring some errors; on the other hand, the seasonality of submesoscale motion may be another mechanism for this different KE cascade (Rocha et al., 2016; Lin et al., 2020). Thus, the accuracy of energy fluxes needs to be improved by more fine and long-term observations in future study.

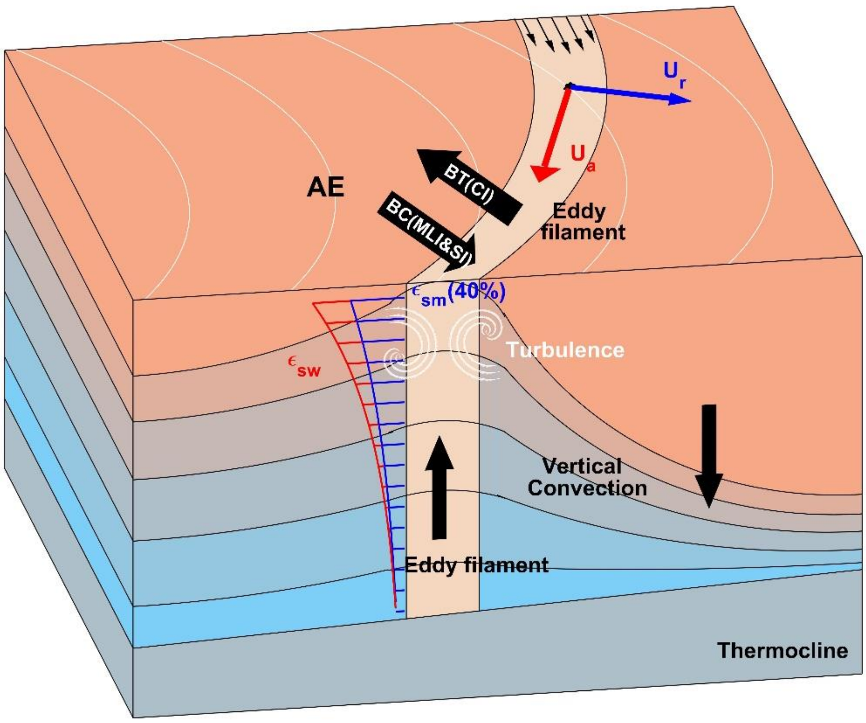

Figure 12. Structural diagram of the energy transfers of the eddy filament in the AE. Upward (downward) arrows are used to represent upwelling (downwelling). U_r represents outward movement of the filament; U_a is the rotational translation velocity of the filament; ε_{sw} and ε_{sm} are wind-wave forced turbulence and submesoscale forced turbulence, respectively; *CI* and *SI* represent centrifugal and symmetric instabilities; *MLI* represents mixed-layer baroclinic instability. *BC* and *BT* are the baroclinic and barotropic energy conversion.

5 Conclusion

In this study, we investigated the three-dimensional structure of an eddy filament within an AE using MVP300 and VMP measurements in the western SCS in August 2021. The eddy filament with 4-km width was generated on August 15$^{\text{th}}$, and rotated at an angular velocity of $\frac{\pi}{8}$ rad/day. The filament had high-salinity and low-temperature properties. And it had a strong secondary vertical current, which promoted the high chlorophyll-a concentrations belt.

Enhanced turbulent dissipation rate were observed within the filament. The turbulent dissipation rate parameterized by *SI* was higher than the in-situ value. Based on energy budget analysis of submesoscale instability, we found that the filament transferred KE to the mesoscale eddy via barotropic instability. Meanwhile, *HRS* was always negative, thus reduced the downward KE transfers. Types of submesoscale instability showed that *CI* rather than *SI* dominated the filament zone. Hence, we inferred the overestimation of turbulent dissipation rates was induced by *CI*. This study directs us a new turbulent scheme including *CI* is needed in future study.

Acknowledgments

This study was supported by the National Natural Science Foundation of China (Grant No. 41976002, No. 42227901) and Project of the Southern Marine Science and Engineering Guangdong Laboratory (Zhuhai) (Grant No. SML2021SP205). We are grateful to all the members on the "Xiangyanghong 3" R/V cruise.

References

Bayler, E. J., & Liu, Z. (2008). Basin-scale wind-forced dynamics of the seasonal southern South China Sea gyre. *Journal of Geophysical Research: Oceans*, 113(C7). https://doi.org/10.1029/2007JC004519

Belcher, S. E., Grant, A. L., Hanley, K. E., Fox-Kemper, B., Van Roekel, L., Sullivan, P. P., Large, W.G., Brown, A., Hines, A., Calvert, D., Rutgersson, A., Pettersson, H., Bidlot, J.R., Janssen, P. A. & Polton, J. A. (2012). A global perspective on Langmuir turbulence in the ocean surface boundary layer. *Geophysical Research Letters*, 39(18). https://doi.org/10.1029/2012GL052932

Bennetts, D. A., & Hoskins, B. J. (1979). Conditional symmetric instability-a possible explanation for frontal rainbands. *Quarterly Journal of the Royal Meteorological Society*, 105(446), 945-962. https://doi.org/10.1002/qj.49710544615

Boccalett, G., Ferrari, R., & Fox-Kemper, B. (2006). Mixed layer instabilities and restratification. *Journal of Physical Oceanography*, 37, DOI: 10.1175/JPO3101.1.

Böning, C. W., & Budich, R. G. (1992). Eddy dynamics in a primitive equation model: Sensitivity to horizontal resolution and friction. *Journal of Physical Oceanography*, 22(4), 361-381. https://doi.org/10.1175/1520-0485(1992)022<0361:EDIAPE>2.0.CO;2

Brannigan, L. (2016). Intense submesoscale upwelling in anticyclonic eddies. *Geophysical Research Letters*, 43(7), 3360-3369. https://doi.org/10.1002/2016GL067926

Brannigan, L., Marshall, D. P., Garabato, A. C. N., Nurser, A. G., & Kaiser, J. (2017). Submesoscale instabilities in mesoscale eddies. *Journal of Physical Oceanography*, 47(12), 3061-3085. https://doi.org/10.1175/JPO-D-16-0178.1

Buckingham, C. E., Lucas, N. S., Belcher, S. E., Rippeth, T. P., Grant, A. L., Le Sommer, J., ... & Naveira Garabato, A. C. (2019). The contribution of surface and submesoscale processes to turbulence in the open ocean surface boundary layer. *Journal of Advances in Modeling Earth Systems*, 11(12), 4066-4094. https://doi.org/10.1029/2019MS001801

Capet, X., McWilliams, J. C., Molemaker, M. J., & Shchepetkin, A. F. (2008). Mesoscale to submesoscale transition in the California Current System. Part III: Energy balance and flux. *Journal of Physical Oceanography*, 38(10), 2256-2269. https://doi.org/10.1175/2008JPO3810.1

Callies, J., & Ferrari, R. (2013). Interpreting energy and tracer spectra of upper-ocean turbulence in the submesoscale range (1–200 km). *Journal of Physical Oceanography*, 43(11), 2456-2474. https://doi.org/10.1175/JPO-D-13-063.1

Chen, Y., Li, Q. P., & Yu, J. (2022). Submesoscale variability of subsurface chlorophyll-a across eddy-driven fronts by glider observations. *Progress in Oceanography*, 209, 102905. doi:10.1016/j.pocean.2022.102905

Chu, P. C., Edmons, N. L., & Fan, C. (1999). Dynamical mechanisms for the South China Sea seasonal circulation and thermohaline variabilities. *Journal of Physical Oceanography*, 29(11), 2971-2989. https://doi.org/10.1175/1520-0485(1999)029<2971:DMFTSC>2.0.CO;2

D'asaro, E., Lee, C., Rainville, L., Harcourt, R., & Thomas, L. (2011). Enhanced turbulence and energy dissipation at ocean fronts. *Science*, 332(6027), 318-322. https://doi.org/10.1126/science.1201515

Dong, J., Fox-Kemper, B., Jing, Z., Yang, Q., Tian, J., & Dong, C. (2022). Turbulent dissipation in the surface mixed layer of an anticyclonic mesoscale eddy in the South China Sea. *Geophysical Research Letters*, e2022GL100016. https://doi.org/10.1029/2022GL100016

Dong, J., Fox-Kemper, B., Zhang, H., & Dong, C. (2021). The scale and activity of symmetric instability estimated from a global submesoscale-permitting ocean model. *Journal of Physical Oceanography*, 51(5), 1655-1670. https://doi.org/10.1175/JPO-D-20-0159.1

Dong, J., & Zhong, Y. (2018). The spatiotemporal features of submesoscale processes in the northeastern South China Sea. *Acta Oceanologica Sinica*, 37, 8-18. https://doi.org/10.1007/s13131-018-1277-2

Emanuel, K. A. (1979). Inertial instability and mesoscale convective systems, Part I: Linear theory of inertial instability in rotating viscous fluids. *Journal of the Atmospheric Sciences*, 36, 2425–2449.

Fang, W., Fang, G., Shi, P., Huang, Q., & Xie, Q. (2002). Seasonal structures of upper layer circulation in the southern South China Sea from in situ observations. *Journal of Geophysical Research: Oceans*, 107(C11), 23-1. https://doi.org/10.1029/2002JC001343

Fer, I., Peterson, A. K., & Ullgren, J. E. (2014). Microstructure measurements from an underwater glider in the turbulent Faroe Bank Channel overflow. *Journal of Atmospheric and Oceanic Technology*, 31(5), 1128-1150. https://doi.org/10.1175/JTECH-D-13-00221.1

Fox-Kemper, B., Ferrari, R., & Hallberg, R. (2008). Parameterization of mixed layer eddies. Part I: Theory and diagnosis. *Journal of Physical Oceanography*, 38(6), 1145-1165. https://doi.org/10.1175/2007JPO3792.1

Gan, J., & Qu, T. (2008). Coastal jet separation and associated flow variability in the southwest South China Sea. *Deep Sea Research, Part I*, 55, 1–19, doi:10.1016/j.dsr.2007.09.008.

Gula, J., Molemaker, M., & McWilliams, J (2014). Submesoscale cold filaments in the Gulf Stream. Journal of Physical Oceanography, 44, 2617–2643. https://doi.org/10.1175/JPO-D-14-0029.1

Hoskins, B. J. (1974). The role of potential vorticity in symmetric stability and instability. *Quarterly Journal of the Royal Meteorological Society*, 100(425), 480-482. https://doi.org/10.1002/qj.49710042520

Gula, J., Taylor, J., Shcherbina, A., & Mahadevan, A. (2022). Chapter 8 - Submesoscale processes and mixing. *Ocean Mixing*, M. Meredith and A. Naveira Garabato, Eds., Elsevier, 181–214.

Hu, J., Gan, J., Sun, Z., Zhu, J., & Dai, M. (2011). Observed three-dimensional structure of a cold eddy in the southwestern South China Sea. *Journal of Geophysical Research*, 116, C05016. doi:10.1029/2010JC006810.

Huang, X., Jing, Z., Zheng, R., & Cao, H. (2020). Dynamical analysis of submesoscale fronts associated with wind-forced offshore jet in the western South China Sea. *Acta Oceanologica Sinica*, 39, 1-12. https://doi.org/10.1007/s13131-020-1671-4

Jensen, M.F. (2016). Glacial ocean circulation and stratification explained by reduced atmospheric temperature. *Proceedings of the National Academy of Sciences of the United States of America*, https://doi.org/10.1073/pnas.161043811

Jing, Z., Fox-Kemper, B., Cao, H., Zheng, R., & Du, Y. (2021). Submesoscale fronts and their dynamical processes associated with symmetric instability in the Northwest Pacific subtropical ocean. *Journal of Physical Oceanography*, 51(1), 83-100. https://doi.org/10.1175/JPO-D-20-0076.1

Legg, S., McWilliams, J., & Gao, J (1998). Localization of deep ocean convection by a mesoscale eddy. *Journal of Physical Oceanography*, 28, 944-970. https://doi.org/10.1175/1520-0485(1998)028<0944:LODOCB>2.0.CO;2

Lehahn, Y., d'Ovidio, F., Lévy, M., Heifetz, E (2007). Stirring of the northeast Atlantic spring bloom: A Lagrangian analysis based on multisatellite data. *Journal of Geophysical Research: Oceans*, 112, C08005, https://doi.org/10.1029/2006JC003927

L'Hégaret, P., Schütte, F., Speich, S., Reverdin, G., Baranowski, D.B., Czeschel, R., Fischer, T., Foltz, G.R., Heywood, K. J., Krahmann, G., Laxenaire, R., Bihan, C. L., Bot, P.L., Leizour, S., Rollo, C., Schlundt, M., Siddle, E., Subirade, C., Zhang, D., & Karstensen, J. (2023). Ocean cross-validated observations from R/Vs L'Atalante, Maria S. Merian, and Meteor and related platforms as part of the EUREC4A-OA/ATOMIC campaign. *Earth System Science Data*, 15, 1801–1830, https://doi.org/10.5194/essd-15-1801-2023.

Lin, H., Liu, Z., Hu, J., Menemenlis, D., & Huang, Y. (2020). Characterizing meso-to submesoscale features in the South China Sea. *Progress in Oceanography*, 188, 102420. https://doi.org/10.1016/j.pocean.2020.102420

Martin, A., & Richards, K. (2001). Mechanisms for vertical nutrient transport within a North Atlantic mesoscale eddy. *Deep Sea Research Part I: Oceanographic Research Papers*, 48, 757–773.

McWilliams, J. C., Sullivan, P. P., & Moeng, C. H. (1997). Langmuir turbulence in the ocean. *Journal of Fluid Mechanics*, 334, 1-30. https://doi.org/10.1017/S0022112096004375

McWilliams, J. (2016). Submesoscale currents in the ocean. *Proceedings of the Royal Society A*, 472, 20160117. http://dx.doi.org/10.1098/rspa.2016.0117

Melander, M. V., McWilliams, J. C., & Zabusky, N. J. (1987). Axisymmetrization and vorticity-gradient intensification of an isolated two-dimensional vortex through filamentation. *Journal of Fluid Mechanics*, 178, 137-159. https://doi.org/10.1017/S0022112087001150

Montgomery, M. T., & Enagonio, J. (1998). Tropical cyclogenesis via convectively forced vortex Rossby waves in a three-dimensional quasigeostrophic model. *Journal of the atmospheric sciences*, 55(20), 3176-3207. https://doi.org/10.1175/1520-0469(1998)055<3176:TCVCFV>2.0.CO;2

Montgomery, M. T., & Kallenbach, R. J. (1997). A theory for vortex Rossby-waves and its application to spiral bands and intensity changes in hurricanes. *Quarterly Journal of the Royal Meteorological Society*, 123(538), 435-465. https://doi.org/10.1002/qj.49712353810

Möller, J. D., & Montgomery, M. T. (1999). Vortex Rossby waves and hurricane intensification in a barotropic model. *Journal of the atmospheric sciences*, 56(11), 1674-1687. https://doi.org/10.1175/1520-0469(1999)056<1674:VRWAHI>2.0.CO;2

Möller, J. D., & Montgomery, M. T. (2000). Tropical cyclone evolution via potential vorticity anomalies in a three-dimensional balance model. *Journal of the atmospheric sciences*, 57(20), 3366-3387. https://doi.org/10.1175/1520-0469(2000)057<3366:TCEVPV>2.0.CO;2

Ni, Q., Zhai, X., Wilson, C., Chen, C., & Chen, D. (2021). Submesoscale eddies in the South China Sea. *Geophysical Research Letters*, 48(6), e2020GL091555. https://doi.org/10.1029/2020GL091555

Qi, Y., Shang, C., Mao, H., Qiu, C., Shang, X. (2020). Spatial structure of turbulent mixing of an anticyclonic mesoscale eddy in the northern South China Sea. *Acta Oceanologica Sinica*, 39(11), 69-81. https://doi.org/10.1007/s13131-020-1676-z

Qiu, B., Nakano, T., Chen, S., & Klein, P. (2022a). Bi-Directional Energy Cascades in the Pacific Ocean From Equator to Subarctic Gyre. *Geophysical Research Letters*, 49(8), e2022GL097713. https://doi.org/10.1029/2022GL097713

Qiu, B., Chen, S., Klein, P., Wang, J., Torres, H., Fu, L. L., & Menemenlis, D. (2018). Seasonality in transition s*cale from balanced to unbalanced motions in the world ocean.* Journal of Physical Oceanography, 48(3), 591-605. https://doi.org/10.1175/JPO-D-17-0169.1

Qiu, C., Mao, H., Liu, H., Xie, Q., Yu, J., Su, D., ... & Lian, S. (2019). Deformation of a warm eddy in the northern South China Sea. *Journal of Geophysical Research: Oceans*, 124(8), 5551-5564. https://doi.org/10.1029/2019JC015288

Qiu, C., Ouyang, J., Yu, J., Mao, H., Qi, Y., Wu, J., & Su, D. (2020). Variations of mesoscale eddy SST fronts based on an automatic detection method in the northern South China Sea. *Acta Oceanologica Sinica*, 39(11), 82-90. https://doi.org/10.1007/s13131-020-1669-y

Qiu, C., Yang, Z., Wang, D., Feng, M., & Su, J. (2022). The enhancement of submesoscale ageostrophic motion on the mesoscale eddies in the South China Sea. *Journal of Geophysical Research: Oceans*, e2022JC018736. https://doi.org/10.1029/2022JC018736

Rocha, C., Gille, S., Chereskin, T., & Menemenlis, D. (2016). Seasonality of submesoscale dynamics in the Kuroshio Extension. *Geophysical Research Letter*, 43, 11,304–11,311, doi:10.1002/2016GL071349

Ruiz, S., Claret, M., Pascual, A., Olita, A., Troupin, C., Capet, A., ... & Mahadevan, A. (2019). Effects of oceanic mesoscale and submesoscale frontal processes on the vertical transport of phytoplankton. *Journal of Geophysical Research: Oceans*, 124(8), 5999-6014. https://doi.org/10.1029/2019JC015034

Shao, M., Ortiz-Suslow, D. G., Haus, B. K., Lund, B., Williams, N. J., Ozgokmen, T. M., Laxague, N.J.M., Horstmann, J., & Klymak, J.M. (2019). The variability of winds and fluxes observed near submesoscale fronts. *Journal of Geophysical Research: Oceans*, 124, 7756–7780. https://doi.org/10.1029/2019JC015236

Song, X., Xie, X., Qiu, B., Cao, H., Xie, S. P., Chen, Z., & Yu, W. (2022). Air-Sea Latent Heat Flux Anomalies Induced by Oceanic Submesoscale Processes: An Observational Case Study. *Frontiers in Marine Science*, 9. https://doi.org/10.3389/fmars.2022.850207

Srinivasan, K., Barkan, R., & McWilliams, J. C. (2023). A forward energy flux at submesoscales driven by frontogenesis. *Journal of Physical Oceanography*, 53(1), 287-305. https://doi.org/10.1175/JPO-D-22-0001.1

Su, Z., Torres, H., Klein, P., Thompson, A. F., Siegelman, L., Wang, J., ... & Hill, C. (2020). High-frequency submesoscale motions enhance the upward vertical heat transport in the global ocean. *Journal of Geophysical Research: Oceans*, 125(9), e2020JC016544. https://doi.org/10.1029/2020JC016544

Tang, H., Shu, Y., Wang, D., Xie, Q., Zhang, Z., Li, J., ... & Liu, D. (2023). Submesoscale processes observed by high-frequency float in the western South China sea. *Deep Sea Research Part I: Oceanographic Research Papers*, 192, 103896. https://doi.org/10.1016/j.dsr.2022.103896

Taylor, J. R., & Ferrari, R. (2010). Buoyancy and wind-driven convection at mixed layer density fronts. *Journal of Physical Oceanography*, 40(6), 1222-1242. https://doi.org/10.1175/2010JPO4365.1

Taylor, J.R., Bachman, S., Stamper, M., Hosegood, P., Adams, K., Salle, J. & Torres, R. (2018). Submesoscale Rossby waves on the Antarctic circumpolar current. *Science Advances*, 4, eaao2884.

Thomas, L. N., Taylor, J. R., Ferrari, R., & Joyce, T. M. (2013). Symmetric instability in the Gulf Stream. *Deep Sea Research Part II: Topical Studies in Oceanography*, 91, 96-110. https://doi.org/10.1016/j.dsr2.2013.02.025

Wang, S., Jing, Z., Wu, L., Cai, W., Chang, P., Wang, H., Geng, T., Danabasoglu, G., Chen, Z., Ma, X., Gan, B., Yang, H. (2022). El Niño/Southern Oscillation inhibited by submesoscale ocean eddies. *Nature Geosciences*, 15, 112–117. https://doi.org/10.1038/s41561-021-00890-2

Wolk, F., Yamazaki, H., Seuront, L., & Lueck, R. G. (2002). A new free-fall profiler for measuring biophysical microstructure. *Journal of Atmospheric and Oceanic Technology*, 19(5), 780-793. https://doi.org/10.1175/1520-0426(2002)019<0780:ANFFPF>2.0.CO;2

Xu, H., Xie, S. P., Wang, Y., Zhuang, W., & Wang, D. (2008). Orographic effects on South China Sea summer climate. *Meteorology and Atmospheric Physics*, 100(1), 275-289. https://doi.org/10.1117/12.730375

Xuan, J., Ding, R., Ni, X., Huang, D., Chen, J., & Zhou, F. (2021). Wintertime Submesoscale Offshore Events Overcoming Wind-Driven Onshore Currents in the East China Sea. *Geophysical Research Letters*, 48(23), e2021GL095139. https://doi.org/10.1029/2021GL095139

Yang, Q., Nikurashin, M., Sasaki, H., Sun, H., & Tian, J. (2019). Dissipation of mesoscale eddies and its contribution to mixing in the northern South China Sea. *Scientific Reports*, 9(1), 556. https://doi.org/10.1038/s41598-018-36610-x

Yang, Q., Zhao, W., Liang, X., Dong, J., & Tian, J. (2017). Elevated mixing in the periphery of mesoscale eddies in the South China Sea. *Journal of Physical Oceanography*, 47(4), 895-907. https://doi.org/10.1175/JPO-D-16-0256.1

Yu, X., Naveira Garabato, A. C., Martin, A. P., Buckingham, C. E., Brannigan, L., & Su, Z. (2019). An annual cycle of submesoscale vertical flow and restratification in the upper ocean. *Journal of Physical Oceanography*, 49(6), 1439-1461. https://doi.org/10.1175/JPO-D-18-0253.1

Zhang, J., Zhang, Z., Qiu, B., Zhang, X., Sasaki, H., Zhao, W., & Tian, J. (2021). Seasonal modulation of submesoscale kinetic energy in the upper ocean of the northeastern South China Sea. *Journal of Geophysical Research: Oceans*, 126(11), e2021JC017695. https://doi.org/10.1029/2021JC017695

Zhang, Z., & Qiu, B. (2018). Evolution of submesoscale ageostrophic motions through the life cycle of oceanic mesoscale eddies. *Geophysical Research Letters*, 45(21), 11-847. https://doi.org/10.1029/2018GL080399

Zhang, Z., & Qiu, B. (2020). Surface chlorophyll enhancement in mesoscale eddies by submesoscale spiral bands. *Geophysical Research Letters*, 47(14), e2020GL088820. https://doi.org/10.1029/2020GL088820

Zheng, R., & Jing, Z. (2022). Submesoscale-enhanced filaments and frontogenetic mechanism within mesoscale eddies of the South China Sea. *Acta Oceanologica Sinica*, 41(7), 1-12. https://doi.org/10.1007/s13131-021-1971-3

Zhong, Y., Bracco, A., Tian, J., Dong, J., Zhao, W., & Zhang, Z. (2017). Observed and simulated submesoscale vertical pump of an anticyclonic eddy in the South China Sea. *Scientific Reports*, 7(1), 44011. https://doi.org/10.1038/srep44011

Zu, T., Wang, D., Wang, Q., Li, M., Wei, J., Geng, B., He, Y., & Chen, J. (2020). A revisit of the interannual variation of the South China Sea upper layer circulation in summer: Correlation between the eastward jet and northward branch. *Climate Dynamics*, 54(1), 457-471. https://doi.org/10.1007/s00382-019-05007-5